Exp Fluids (2012) 53:1301–1316
DOI 10.1007/s00348-012-1361-x

RESEARCH ARTICLE

Droplet collision mixing diagnostics using single fluorophore LIF

Brian Carroll · Carlos Hidrovo

Received: 19 December 2011 / Revised: 30 July 2012 / Accepted: 1 August 2012 / Published online: 19 August 2012

Abstract A novel droplet mixing measurement technique is presented that employs single fluorophore laser-induced fluorescence, custom image processing, and statistical analysis for monitoring and quantifying mixing in confined, high-speed droplet collisions. The diagnostic procedure captures time-varying fluorescent signals following binary droplet collisions and reconstructs the spatial concentration field by relating fluorophore intensity to relative concentration. Mixing information is revealed through two governing statistics that separate the roles of convective rearrangement and molecular diffusion during the mixing process. The end result is a viewing window into the rich dynamics of droplet collisions and a diagnostic tool that differentiates between poor and effective mixing. The technique has proved invaluable in the laboratory by allowing direct comparison of different hydrodynamic conditions, such as collision Reynolds and Peclet number, and collision geometries, such as T and Y-junctions. Experiments indicate improved mixing rates and degree of homogenization as the convective timescale for the collision is decreased. Visualization of mixing residuals using pseudo color mapping also identifies areas that are largely segregated from the mixing process, resulting in islands where mixing is poor and stirring has proved ineffective. As the collision velocity is increased, vortical flow fields become apparent and mixing is greatly improved.

B. Carroll (✉) · C. Hidrovo
Multiscale Thermal Fluids Laboratory,
University of Texas at Austin, Austin, TX, USA
e-mail: brian.carroll@utexas.edu

C. Hidrovo
e-mail: hidrovo@mail.utexas.edu

1 Introduction

Mixing, dilution, or sample homogenization are an essential process in modern lab-on-a-chip (LOC) and micro-total analysis systems (μTAS) where this seemingly simple task remains a major obstacle. The topic is forefront at any microfluidics; conference or periodical and complete books are devoted to the subject (Nguyen 2008). The ability to analyze non-equilibrium conditions and probe the kinetics of bio-molecular reactions has been limited by the speed at which mixing takes place. The low Reynolds (*Re*) numbers typical of most microfluidic devices signify laminar and orderly flows that are devoid of any inertial characteristics. The turbulent flow regime exploited at the macroscale for fast mixing is difficult and impractical to implement in microscale flows, although turbulent flow has been achieved for continuous flow microfluidic devices (Takahashi et al. 1995). Droplet-based systems offer significant advantages over their continuous flow counterparts, such as reduced product dispersion and sample consumption and the ability to precisely control and monitor reactions at desired timescales. However, the microsecond mixing times that have been achieved for continuous flow systems (Knight et al. 1998; Hertzog et al. 2004, 2006) are two orders of magnitude smaller than the state of the art for droplet-based systems (Song et al. 2003, 2006; Song and Ismagilov 2003). Many important structural events, such as nucleotide-flipping (Robinson et al. 2010) and calmodulin (CaM) dynamics (Park et al. 2007), occur on timescales much less than a millisecond. For droplet-based systems, the most common fast mixing technique is chaotic advection. Chaotic advection produces highly divergent particle motion inside droplet volumes using either active or passive means. Regardless of the mixing technique, the overarching goal is rapid and controllable reduction in the effective mass

diffusion length. The faster this length scale is reduced, the faster the mixture is homogenized.

The difficulty in determining the extent or degree of mixing is that there is no unifying theory that clearly distinguishes a "fully mixed" condition. Some (Ottino 1989, 1990, 1994; Dutta and Chevray 1994; Ottino and Wiggins 2004) have applied a Hamiltonian perspective to mixing that describes well-mixed conditions if every particle explores the mixing domain while losing track of each other. This idea of particle divergence is the foundation of chaotic mixing, a concept first pioneered by Aref (1984). This purely dynamical approach to mixing is well suited for high Peclet number laminar flows. Chemists describe well-mixed conditions by the degree in which a chemical reaction takes place, since a reaction cannot proceed unless there are molecular interactions between the reactants (Kling and Mewes 2010). This requires molecular scale proximity. The turbulence community predicts mixed conditions based on the homogenization of a scalar field, such as concentration or temperature (Dimotakis et al. 1983; Koochesfahani and Dimotakis 1986; Dimotakis 2005). If homogenization is poor at the large scale, mixing at the molecular scale will be highly localized and largely poor throughout the volume. If homogenization is complete at sub-system length scales, mixed conditions at the molecular scale, although not guaranteed, may be safely assumed. A mixing system displaying fast homogenization rates at these intermediate, sub-system length scales therefore provides molecularly mixed conditions faster than a similarly scaled system displaying slow homogenization rates. Thus, quantifying the extent of mixing based on concentration field homogenization provides an important metric in mixing system performance and a benchmark for system design. This report describes an optical diagnostic technique that employs laser-induced fluorescence (LIF) using a single fluorophore, unique mixing statistics, and custom image processing to quantify and visualize the extent of mixing in confined droplet collisions.

This newly applied LIF measurement technique was developed for mixing characterization of a recently proposed inertial mixing device that increases droplet mixing rates through high-speed collisions in a confined microchannel (Carroll and Hidrovo 2010, 2011). An easily integrated, chemically inert diagnostic procedure was sought that enables direct comparison of mixing occurring at various inertial conditions The design capitalizes on a rapid mixing technique presented by Simpson et al. (1983, 1986) where microdroplets are collided in an unconfined, gaseous environment at high speed to yield mixing times near 200 μs. Referring to the simplified schematic in Fig. 1, liquid droplets of *Solute 1* and *2* are detached and accelerated by a high-speed gas flow from two opposing legs of a T-junction. Each droplet obtains kinetic energy

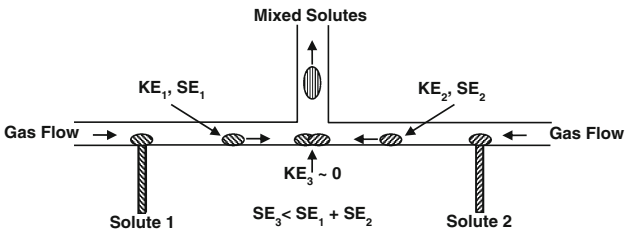

Fig. 1 Shown above is a simplified schematic of an inertial mixing droplet collider. Two droplets with kinetic energy KE_1 and KE_2 and surface energy SE_1 and SE_2 collide at a channel junction. The kinetic energy following collision is essentially zero while the surface energy SE_3 is about $2^{1/3}$ times less for equally sized spherical droplets. The decrease in kinetic and surface energy is viscously dissipated inside the droplet and quickly rearranges the contents for accelerated mixing

KE_1 and KE_2 and surface energy SE_1 and SE_2. At the common junction, the droplets collide and coalesce. The kinetic and surface energy following collision is KE_3 and SE_3, each of which is less than the respective energy prior to collision. This abrupt change in kinetic and surface energy is viscously dissipated through complex velocity fields and bulk volumetric rearrangement. The result is near millisecond mixing for nanoliter-sized droplets. Droplet mixing through confined collisions distinguishes this technique from droplet mixing achieved using boundary interactions.

2 Background

The fast time scales, small length scales, and largely Lagrangian nature of advanced droplet mixing techniques make optical diagnostics the obvious choice for understanding, characterizing, and quantifying mixing dynamics. Within the optical diagnostic tool box, three major techniques have been successfully demonstrated: infrared absorption (IR), spontaneous Raman scattering (SRS), and LIF. IR techniques measure the wavelength and intensity of mid-infrared (2.5–50 μm) light absorbed by a sample. Energy provided by the light source excites molecular vibrations to higher energy levels resulting in absorption bands that are characteristic of specific types of chemical bonds. SRS is an inelastic radiative scattering process that operates on the short lived "virtual" states and subsequent Raman shift. Both IR and SRS provide molecular fingerprints of chemical species present in the investigation region such that the local concentrations are resolved. LIF is also an inelastic radiative process but is based on the absorption and subsequent emission of a photon following quantum energy state interactions. By controlling environmental conditions and using spectral filtering, the LIF signal can be used to construct a spatial concentration map and provide mixing information.

The advantage and limitation of each method rests on the process being investigated. Both IR and SRS suffer from small collision cross sections and therefore produce low-signal intensities unless high-power lasers are used. Furthermore, IR has the disadvantage of line of sight averaging where the received signal is axially integrated. SRS requires a high degree of laser rejection in order to separate the weak, inelastically scattered Raman light from the intensely scattered Rayleigh light that lies close to the laser line (Schrader et al. 1991). Additionally, IR and SRS are a point- or line-based process and a special setup is required to acquire information in two dimensions (Masca et al. 2006; Jendrzok et al. 2010). LIF, on the other hand, readily provides intensity information across a plane and, depending on the optical systems used, only weakly integrates the third dimension. Compared with IR and SRS, LIF provides a significantly greater collision cross section such that the excitation energy required for a detectable signal is significantly less and in many cases a conventional white light source is sufficient. The difficulty in discerning mixing information using fluorescent intensity is that the fluorescent emission signal is often dependent on environmental conditions, such as temperature and pressure; mixture conditions, such as pH; and excitation source stability, such as temporal and spatial non-uniformities. These variables attenuate and skew the concentration-dependent signal such that mixing information is lost or misleading. However, for investigating mixing in microfluidic devices, LIF remains the most suitable method given the small length and time scales and ease of system integration.

LIF has heritage in many diverse science and engineering applications. Initial success as a laser dye was quickly advanced to a method for studying molecular collisions and quantifying molecular concentrations with detection efficiencies comparable to mass spectrometers at that time (Kinsey 1977). Over the past four decades, LIF has evolved into an invaluable optical diagnostic tool. It has allowed investigation of complex structures not possible using other visualization techniques, such as mixture composition in reacting and non-reacting shear layers (Koochesfahani and Dimotakis 1986), turbulent jets (Dimotakis, et al. 1983), and combustion processes (Matsumoto et al. 1999). LIF allows spatial resolutions greater than the light diffraction limit through Förster Resonance Energy Transfer and has opened up new opportunities in microbiology previously unachievable (Quercioli 2011). The often complex dependence of fluorescent intensity to mixture composition and environmental conditions has allowed LIF measurements of temperature (Anderson et al. 1998; Coppeta and Rogers 1998; Lavieille et al. 2001; David et al. 2006), pressure (Hiller and Hanson 1988), pH levels (Bellerose and Rogers 1994; Coppeta and Rogers 1998), film thickness (Coppeta et al. 1996; Hidrovo and Hart 2001), velocity distribution functions (Jacobs et al. 2007), and molecular level mixing (Bellerose and Rogers 1994; Faes and Glasmacher 2010; Kling and Mewes 2010). The LIF application presented herein is the time resolved microscopy visualization of spatial concentration distributions and quantification of mixing homogenization in droplets following high-speed collisions in a confined microchannel. The focus is on passive mixing, where the flow is unaffected by the scalar field yielding Level 1 type mixing (Dimotakis 2005). A single fluorophore dye is used, and the liquid volume illuminated remains at uniform temperature and pH throughout the mixing event.

3 Technique fundamentals

3.1 Fluorescence

Since the emphasis of this manuscript is using LIF to extract mixing information during droplet collisions, only a brief, top-level account of the salient features of the LIF process is provided below. The reader is referred to Arbeloa et al. (1998, 2005) for highly detailed photo-physical and chemical descriptions and Quercioli (2011) for a comprehensive review of fluorescence and its applications in modern microscopy. Fluorescence occurs when a specific type of molecule, called a fluorophore, is excited by a photon and undergoes inelastic rotational and vibrational losses before emitting a photon of longer wavelength and returning to the ground state. Photon emission can be reduced, entirely suppressed, or spectrally altered through non-radiative quenching processes. Such processes include imposed chemical reactions (Ware 1962; Knight et al. 1998; Kling and Mewes 2010), self-quenching due to collisions with like molecules (MacDonald 1990), or specie-dependent bathochromic shifts in the fluorescent band (Arbeloa et al. 2005). For the diagnostic technique presented here, no chemical reactions are imposed or considered and only the self-quenching process is recognized as a possible path for fluorescent attenuation.

As light propagates through a participating medium its intensity decays with distance. The rate of decay is dependent on the spectral properties of the incident light and absorption properties of the participating medium. Water, for instance, preferentially absorbs longer wavelength red light to a greater degree than shorter wavelength blue light. In the case of a fluorescing substance, the absorbed shorter wavelength intensity is released as longer wavelength fluorescence. However, the process is inelastic and only a fraction of the absorbed excitation energy is emitted as fluorescence. The quantum yield of the process is the ratio of emitted fluorescence intensity to absorbed

excitation intensity. To help illustrate this process, consider the control volume shown in Fig. 2, consisting of a fluorescing fluid of infinite height and depth but finite length x. As the excitation light propagates through the volume, there is a decrease in intensity with distance due to specie absorption. The decrease in the excitation intensity I_{Ex} is manifested as an increase in fluorescent intensity I_{Em}, the ratio of which is related to the quantum efficiency, Ψ, of the process:

$$\frac{I_{\mathrm{Em,Out}} - I_{\mathrm{Em,In}}}{I_{\mathrm{Ex,Out}} - I_{\mathrm{Ex,In}}} = -\frac{dI_{\mathrm{Em}}}{dI_{\mathrm{Ex}}} = \Psi \tag{1}$$

The change in excitation intensity is related to the concentration c and extinction coefficient ε of the absorbing specie and decays exponentially with distance x into the participating medium. The ratio of the excitation intensity at some distance x, $I_{Ex,x}$, to the incident intensity at $x = 0$, $I_{Ex,0}$, is expressed by Lambert–Beer's law:

$$\frac{I_{Ex,x}}{I_{Ex,0}} = \exp(-\varepsilon c x) \tag{2}$$

For an aqueous solution with constant extinction coefficient, the change in intensity is determined by:

$$dI_{\mathrm{Ex,x}} = -\varepsilon I_{\mathrm{Ex,0}} \exp(-\varepsilon c x)(c dx + x dc) \tag{3}$$

If the physical length is maintained constant at an interrogation depth l, the change in intensity is determined only by the change in fluorophore concentration:

$$dI_{\mathrm{Ex}} = -I_{\mathrm{Ex,x_0}} \varepsilon l \exp(-\varepsilon c l) dc \tag{4}$$

Cast in these terms, the concentration is appropriately non-dimensionalized by a characteristic system concentration $c_{\mathrm{ch}} = 1/\varepsilon l$:

$$dI_{\mathrm{Ex}} = -I_{\mathrm{Ex,x_0}} \frac{1}{c_{\mathrm{ch}}} \exp\left(\frac{c}{c_{\mathrm{ch}}}\right) dc = -I_{\mathrm{Ex,x_0}} \exp(-c^*) dc^* \tag{5}$$

The ratio of the actual concentration to the characteristic system concentration, c^*, is traditionally labeled as the optical thickness. When the optical thickness is much less than unity, optically thin conditions exist and the change in intensity is approximately linear with concentration. An optical thickness much greater than unity provides optically thick conditions and changes in intensity are non-linear with concentration.

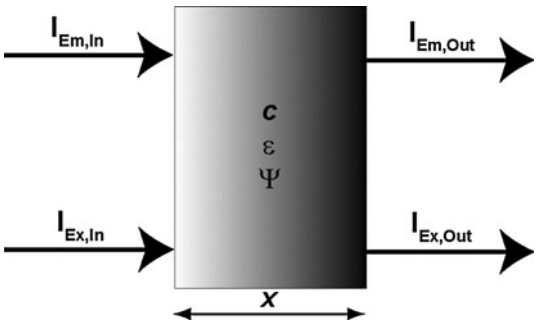

Fig. 2 Control volume used to relate changes in excitation and fluorescent intensity to the participating medium absorption properties

Substituting Eq. 5 into Eq. 1 and integrating gives the following for the fluorescent emission intensity as a function of c^*:

$$I_{\mathrm{Em}} = \Psi I_{\mathrm{Ex,0}}[1 - \exp(-c^*)] \tag{6}$$

Equation 6 is now linearized with respect to c^* to provide a direct link between fluorophore emission and concentration for constant incident excitation intensity:

$$c^* = -\ln\left(1 - \frac{I_{\mathrm{Em}}}{\Psi I_{\mathrm{Ex,0}}}\right) \tag{7}$$

Equation 7 provides a spatial concentration map for each captured image and a snap shot of mixing progress. Mixing is determined complete when the droplet intensity, and hence, concentration is uniform throughout. The absolute concentration, which can be determined by careful calibration of Eq. 7, is unimportant in establishing the state of mixedness.

To test the applicability of Eq. 6, a 230-μm-deep microchannel containing different concentrations of Pyrromethene 556 dissolved in distilled water was imaged for intensity information. This fluorophore was selected for its spectral properties, photo-stability, excellent water solubility, and non-existent tendency to diffuse into the microchannel substrate material (polydimethylsiloxane). Other dyes considered, such as the Rhodamine family, quickly diffuse into the channel walls and increase the background noise level. Data in the literature indicate a quantum yield of 0.73 and an extinction coefficient of 7.2×10^4 cm^{-1}/M (Shah et al. 1990). Using these properties and the optical interrogation depth, the change in fluorescent intensity with concentration is predicted using Eq. 6. The plot in Fig. 3 compares analytical predictions to measured experimental data. There is acceptable agreement up to $c^* \sim 3$. Past this value, higher-order effects that are not captured by the simple analytical model can no longer be neglected. Furthermore, the signal must be monotonic in order to infer relative concentration distributions. This sets an upper limit on the maximum droplet optical thickness at $c^* \sim 3$.

3.2 Spatial intensity statistics

Using intensity statistics to assess the homogenization of a scalar field requires an acute understanding of what the statistics represent in terms of the convective-diffusive mixing dynamics following droplet collisions. This

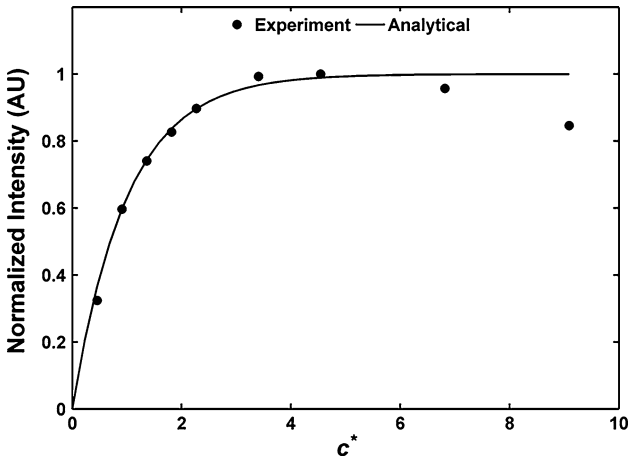

Fig. 3 A comparison of experimental data (*points*) and analytical prediction (*line*) of Pyrromethene 556 fluorescent emission. There is good agreement up to $c^* \sim 3$, after which self-quenching and other higher-order effects not included in the simple analytical model begin to take effect

understanding is facilitated by considering the simple set of images in Fig. 4, each a 400 × 400 pixel array. The pixel intensity values range from 1 (white) to 0 (black) with 256 discrete intensity values (8 bit images). Using the first image in the upper left corner as the initial state of a captured intensity field, two distinct processes can occur: pure convective rearrangement (top row, left to right) or pure diffusion (top row, top to bottom). Convective motion rearranges the contents while maintaining the same discrete intensity values, much like shaking black and white marbles in a can. The images along the top row represent 2, 4, 16, and 64 spatial divisions, respectively. Diffusion maintains the same arrangement but smears the intensity values at the interfaces. To simulate the effects of diffusion, each interior pixel was assigned a new value based on the average intensity of the top, bottom, right, and left neighboring pixels. Starting from the top row of images, each lower image has been spatially averaged 10^1, 10^3, and 10^4 times, respectively. Actual mixing follows a combination of convection and diffusion motion that act in parallel. Fluid properties (Schmidt number) and flow regime (Reynolds number) determine the dominance of one path over the other. Regardless of path taken, visual observation reveals a "more mixed" scalar field as compared to the initial state. It is the objective of the selected statistics to quantify this qualitative visual change in the scalar field.

The statistics that capture the visual representation of scalar mixing are the mean and standard deviation of the global intensity field (system level) and the average gradient of the intensity field (local level). The theoretical expected value of a continuous planar intensity distribution is:

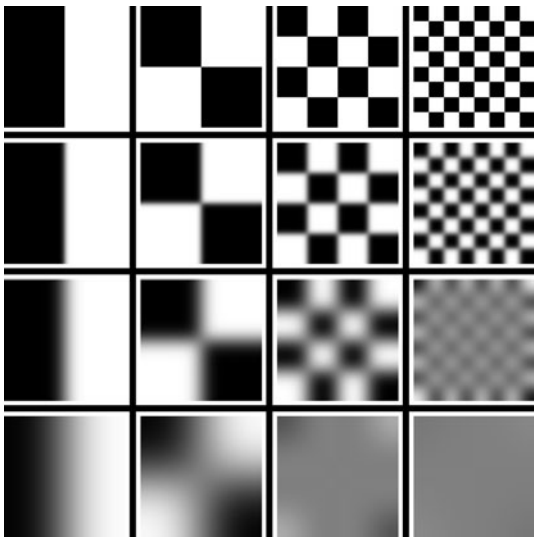

Fig. 4 A series of simple *gray scale* images that illustrate the role of convection and diffusion in mixing. Each of the 16 images is a 400 × 400 pixel array. Starting from the initial distribution in the upper left corner, the pixels can be convectively rearranged by 2^2, 2^4, and 2^6 times (*upper row*) or diffusively averaged 10^1, 10^3, and 10^4 times (*left column*). The remaining three columns represent the same diffusive mixing but starting from a more convectively rearranged state

$$\mu_T = \frac{\int_A I \mathrm{d}A}{A} \tag{8}$$

For digitized images, the intensity values are spatially discrete and the area integral is replaced with a summation over all N pixels inside the mixing volume:

$$\mu = \frac{\sum_{i=1}^{N} I_i}{N} \tag{9}$$

In regards to the images in Fig. 4, the expected value is 0.5 for each image regardless of the mixing path. The average intensity for a closed system, much like the average concentration, is a conserved quantity.

The standard deviation of the intensity field provides a measure of how the spatial intensity values deviate from the expected value μ. In terms of mixing, it is a metric for determining the dispersion of the intensity field. The theoretical standard deviation for a continuous distribution is:

$$\sigma_T = \left[\frac{\int_A (I-\mu)^2 \mathrm{d}A}{A}\right]^{\frac{1}{2}} \tag{10}$$

For discretized samples, the standard deviation is:

$$\sigma = \left[\frac{\sum_{i=1}^{N} (I_i-\mu)^2}{N-1}\right]^{\frac{1}{2}} \tag{11}$$

Since the standard deviation is essentially a measuring stick for variability, it is important to place this measurement in

context with the system being investigated. The standard deviation alone is meaningless without knowledge of the expected value. For instance, a standard deviation of 0.5 for a sample mean of 50 indicates little variability compared with a system with a sample mean of 1. Another complication in using Eq. 9 directly is the dependence of the standard deviation to the magnitude of the intensity values. If results are obtained using an exposure of 10 μs and compared with results using an exposure of 1 μs, the standard deviation would differ even though the actual mixing may be unchanged. This is due to the larger intensity values obtained for slower exposures. Normalizing the standard deviation by the mean value remedies both these issues:

$$\frac{\sigma}{\mu} = \left[\frac{\sum_{i=1}^{N} \left(\frac{I_i}{\mu} - 1 \right)^2}{N-1} \right]^{\frac{1}{2}} \tag{12}$$

The normalized standard deviation is an excellent metric for purely diffusive processes, such as that shown in the column of images where initially the black and white distribution is smeared to a greater degree of gray at the interfaces. The upper right plot in Fig. 5 shows how the normalized standard deviation, σ/μ, decreases as the extent of diffusion is increased from an initial convective distribution along to the top row. If diffusion begins from a much more rearranged state, the degree of mixing is significantly greater for the same number of diffusive averages. This is due to the number of interfaces available for diffusion. However, for the purely convective motion (top row, left to right), the normalized standard deviation remains unchanged even though the images display visually more mixed conditions. This is indicated by the same starting value shown in the top plot in Fig. 5 regardless of the number of spatial divisions considered (2, 4, 16, or 64). Convective rearrangement in the absence of diffusion is not recognized by this statistic since the number of samples and their intensity values remains unchanged. The standard deviation of black and white marbles in a jar remains the same regardless of how vigorously the can is shaken.

In order to capture the convective rearrangement process, a statistic is needed that concerns the local intensity distribution. This is visually conveyed by the number of identifiable interfaces, with more interfaces being indicative of decreasing segregation in non-diffusive tracer fields. These interfaces can be expressed mathematically by the magnitude of the local intensity field divergence and averaged over the entire field:

$$\Phi_T = \frac{\int_A |\nabla I| \mathrm{d}A}{A} \tag{13}$$

For 2D digitized images, the quantity of interest is the magnitude of the gradient in the x and y direction at each pixel location. The average intensity gradient per pixel distance is then:

$$\Phi = \frac{\sum_{i=1}^{N} \left[\left(\frac{\partial I_i}{\partial x} \right)^2 + \left(\frac{\partial I_i}{\partial y} \right)^2 \right]^{\frac{1}{2}}}{N} \tag{14}$$

The partial differential equations are readily computed using a second-order accurate, finite differencing scheme with appropriate padding at the image boundaries. Note that this statistic is keenly similar to a localized standard deviation where the expected value is computed based on a localized pixel subdomain, as opposed to the entire mixing domain.

The lower plot in Fig. 5 shows how the average intensity gradient changes with increasing convective rearrangement. For a purely convective mixing path (top row, left to right), the average gradient increases with increasing number of divisions. The change is negligible, however, for

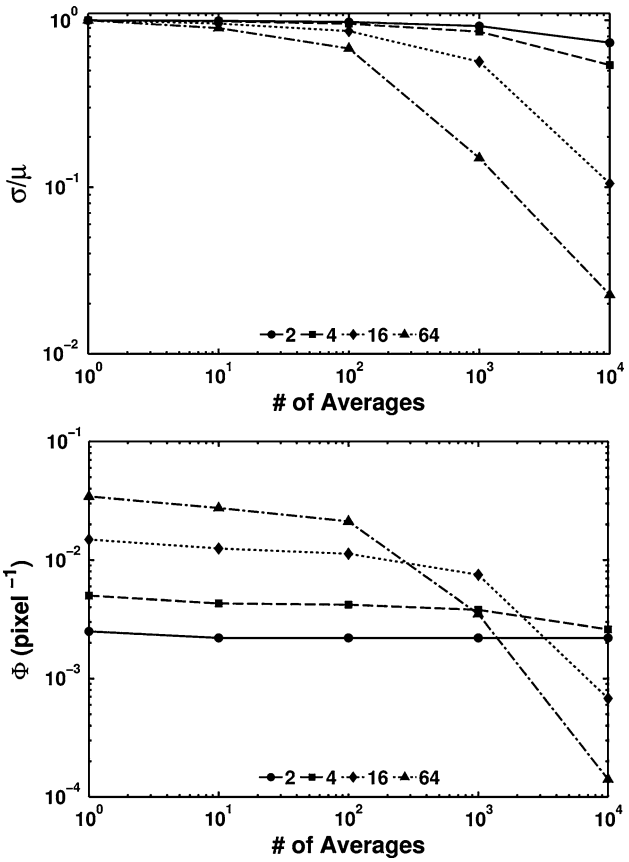

Fig. 5 These plots show how the normalized standard deviation (*top*) and average local intensity gradient (*bottom*) are affected by the degree of diffusive averages for the images shown in Fig. 4. The normalized standard deviation remains unchanged for convective mixing while the average local intensity gradient remains relatively unchanged for diffusive mixing until a high degree of homogenization is reached

a purely diffusive process that begins highly segregated, such as that given by the first two columns of images (2 and 4 divisions). If diffusion begins from a more rearranged state, the average gradient decreases by 2–3 decades (16 and 64 divisions). These results show that convective and diffusive action has opposite effects on the average intensity gradient. It is the role of convection and diffusion to create and smear gradients, respectively. A potentially hazardous interpretation of the average gradient is that a decreasing trend must signify diffusive action. The average gradient continues to grow with increasing convective rearrangement but only until the length scale of each pixel is larger than the actual distance over which the gradient occurs. Even in the absence of diffusion, the average gradient will decrease once the spatial resolution of the measurement system is exceeded.

It is evident based on these simple cases that the standard deviation captures diffusive mixing well but does not recognize spatial rearrangement. This missing metric is provided by the average local gradient that recognizes stirring contributions. Because mixing in most processes of interest is a combination of convective and diffusive paths, using only a single statistic does not provide a complete picture of the mixing event. These two statistics together provide a window into the simultaneous process of convective-diffusive mixing.

3.3 Droplet volume tracking

One of the challenges in applying these statistics to droplet mixing is identification of the droplet volumes, which do not fill the entire image frame and translate across the frame throughout the mixing event. In order to locate each droplet prior to collision, both droplets must emit a detectable signal while maintaining sufficient intensity difference to make the statistics meaningful. This is overcome by using fluorophore concentrations that are an order of magnitude different between the two droplets prior to collision. The captured frames are exported in tagged image format (TIFF) at 12 bit resolution (4,096 intensity levels) and converted to double precision values between 0 and 1. A custom image processing code is executed in MATLAB® to spatially identify the droplet volumes for each frame. The locating algorithm is a combination of noise reduction, local intensity spatial derivatives, intensity thresholding, and shape filling numerical techniques. This process produces a binary region of interest (ROI) mask that is used for confining the mixing statistics to the liquid droplet volumes only. The pairs of images in Fig. 6 illustrate the binary ROI process for an actual mixing event and highlight the volume tracking process. A single droplet of high fluorophore concentration (high intensity) is perched at the apex of a Y-junction (image pair 1). A second droplet

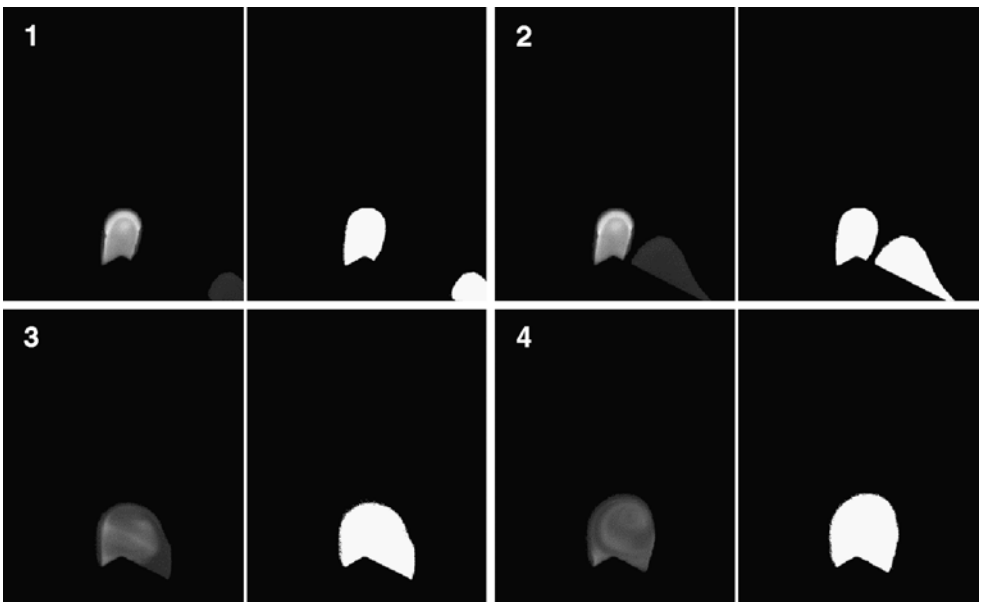

Fig. 6 A series of images of an actual mixing event that illustrates the image processing technique used to identify each droplet volume. Each raw image (*left*) is accompanied by the corresponding binary image (*right*) that shows the droplets in white and clearly identifies the droplet volumes throughout the mixing event. The image sequence shows a droplet perched at the Y-junction apex while second droplet is approaching from lower right (**1**), the moment just prior to collision (**2**), the moment just after collision indicating intensity gradient development (**3**), and the mixing dynamics 1 ms after collision showing the formation of a single vortex with counter-clockwise rotation (**4**)

of lower fluorophore concentration (low intensity) approaches from the lower right (image pair 2) and collides with the first droplet (image pair 3). Mixing takes place within the coalescing droplet (image pair 4). Note the presence of a counter-rotating vortex that is generated as a result of the collision.

4 Experimental setup

The droplet collision mixing device used to demonstrate this diagnostic procedure consists of a T-junction for droplet generation and a Y-junction for droplet collisions. A high-speed air flow (10–20 m/s) is used to create droplets from two liquid streams at opposing T-junctions using techniques previously investigated (Carroll and Hidrovo 2009). The discrete droplets are entrained and transported by the gaseous continuous phase to a common Y-junction where collisions take place at relative velocities near 0.1–1 m/s. The newly coalesced and mixed droplet is then removed from the junction along a common channel, readying the Y-junction for the next colliding droplet pair. Each opposing channel leg is 100 μm wide and the exit channel is 200 μm wide. The depth of each channel is approximately 100 μm. A schematic of the mixing device is shown in Fig. 7. Provided are image sequences that capture the detachment and collision events. The bottom image series shows the growth and detachment of a single

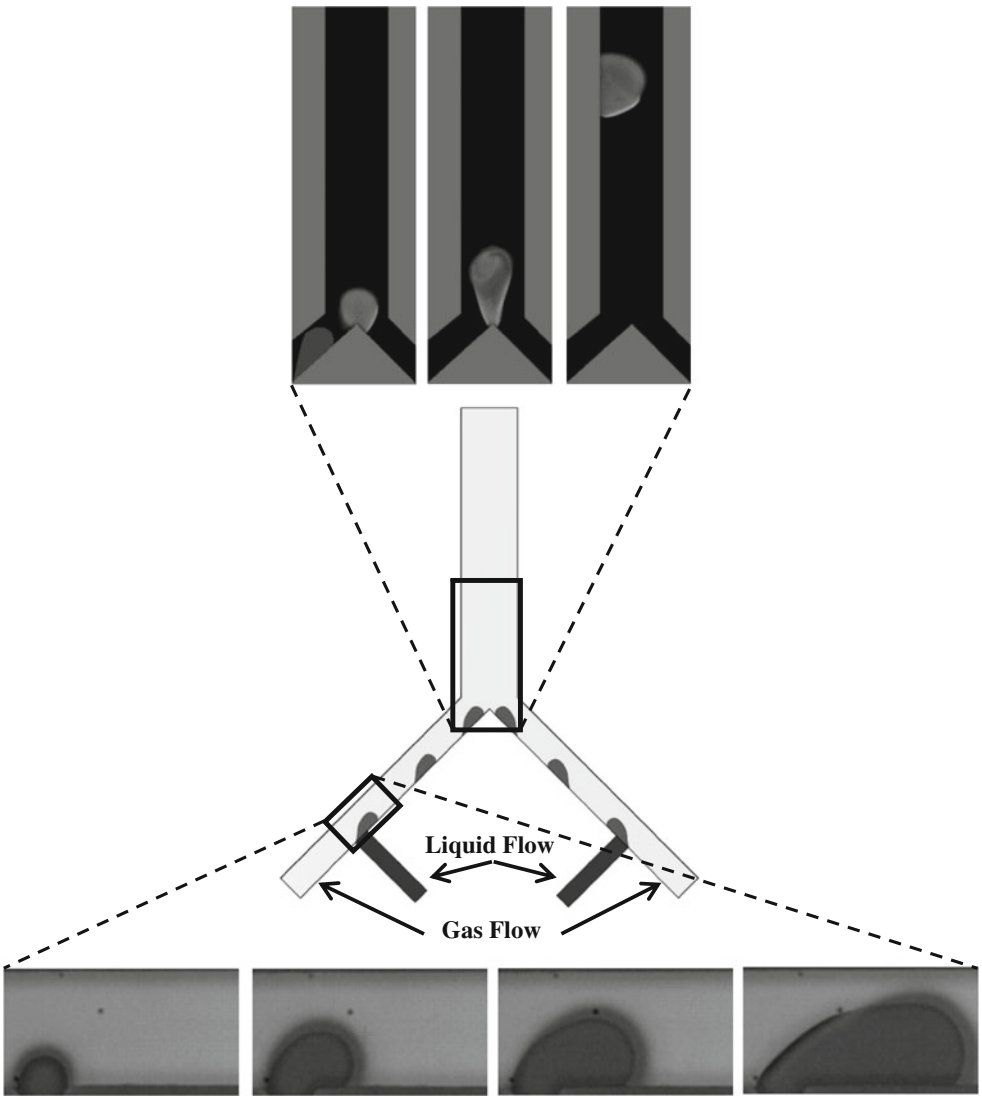

Fig. 7 Top-view CAD schematic of the impact coalescence mixing device accompanying experimental images depicting a collision mixing event (*top*) and the droplet growth and detachment process (*bottom*). The droplet collider uses a high-speed gaseous flow to detach discrete droplets at T-junction. Entrained droplets from two opposing legs are brought together at the apex of a Y-junction. Mixing takes place rapidly and the newly coalesced droplet is removed by the gas flow down a common exit channel

droplet from the left T-junction. In top image sequence, two droplets of high (right) and low (left) fluorophore concentration collide, mix, and exit the junction. Note the difference in intensity of each droplet prior to collision, which is representative of fluorophore concentration.

The impact coalescence mixing device shown in Fig. 7 is microfabricated using standard soft lithography techniques and polydimethylsiloxane (PDMS, Dow Corning Corp.) substrate material. Each PDMS mixing device is bonded using oxygen plasma to a $1'' \times 3''$ standard microscope slide that has been spin coated with a $\sim$5-μm thick layer of PDMS. This ensures all channel walls display the same surface energy and wetting characteristics. Bond strength is improved by post-baking at 65 °C for 8 h. The finished device is then inspected for dimensional integrity using a microscope and checked for leaks using a pressure source and flow meter.

A custom microfluidic test bed has been designed for experimental investigation of multiphase flows, particularly high-speed gas–liquid droplet flows. The test bed consists of pairs of pressure transducers (Validyne P855 Digital Differential Pressure Transmitter) and mass flow sensors (Sierra Smart-Trak2) for real-time data acquisition. Gas flow control is realized using voltage-driven pressure regulators (Proportion-Air QPV1) with feedback control. Compressed air supplied by the facility is oil and particulate filtered and desiccated upstream before being introduced into the pressure regulator. Back pressure is achieved using a 20-turn needle valve (McMaster Carr). Liquid flow control is provided by a constant displacement syringe pump (Harvard Apparatus PHD2000). All instruments and acquisition equipment are routed through a dedicated host computer. A custom LabVIEW Virtual Instrument (National Instruments) provides real-time user control and system diagnostics of all instrumentation. Images of the microfluidic test bed are shown in Fig. 8. The mixing device is secured to the microscope stage, and liquid and gas plumbing is integrated (top image). Two independent gaseous supply circuits are located upstream of mixing device and are used to control the droplet detachment process and droplet collision velocity (bottom image).

Using digitized images to quantify mixing demands that the captured LIF signals are representative of the tracer concentration field. Generating an accurate fluorophore concentration map requires separation emission and excitation frequencies as well as any background noise present in the experimental system. The absorption–emission spectrums of the most common scientific fluorophores are similar in shape but display different Stokes shift lengths (color shift) and excitation and emission spectra broadening. Most commonly available fluorophores display a region where the absorption and emission bands overlap, as shown in Fig. 9 for Pyrromethene 556 (Exciton). In this region, the emission signal is re-absorbed and subsequently re-emitted and does not follow the behavior described by Eq. 7. Signals from this wavelength range should not be included in intensity statistics. Note that the maximum absorption and emission peaks lie in or very close to the overlap region such that operating near these maxima is not always possible. For such conditions, it is recommendable to excite at a shorter wavelength than maximum absorption, especially if the Stokes shift is comparably narrow and there is severe spectra overlap (Borlinghaus 2011).

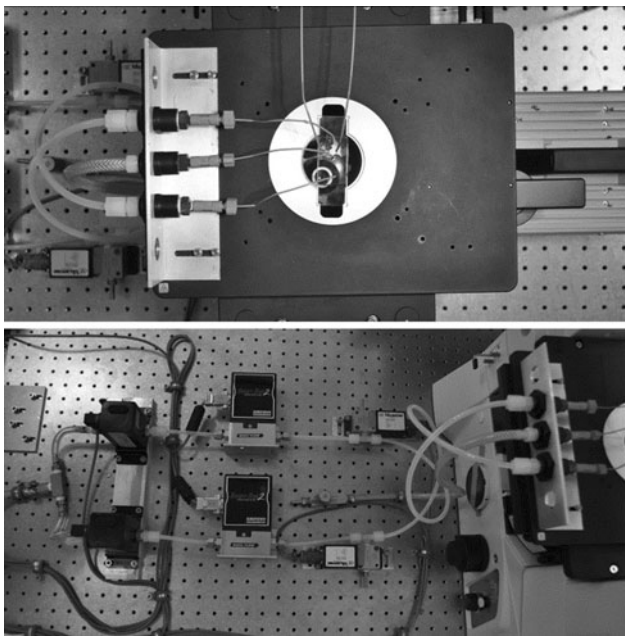

Fig. 8 *Top-view* images of the microfluidic test bench used for investigating gas–liquid microchannel flows. The *upper image* shows microfluidic mixing device secured to microscope stage with integrated gas and liquid delivery *lines*. The *lower image* shows the pressure regulators, flow meters, pressure transducers, and back-pressure valve used for controlling and quantifying gaseous flow. Liquid flow is issued from a constant displacement syringe pump (not shown)

Proper selection of filters and mirrors ensures that the captured signal has not been attenuated by the reabsorption–emission process or generated by sources within the experimental setup. This is accomplished using a carefully specified optical assembly housed inside an epi-fluorescence inverted microscope (Nikon Ti-U). The key components for LIF microscopy are excitation, dichroic, and emission filters that are usually combined into a single block or cube. Referring to the schematic shown in Fig. 10, the 50-nm narrow band pass excitation filter transmits only absorption wavelengths between 450 and 490 nm from the white light source. This ensures that only wavelengths in the non-overlapping absorption band are transmitted. The dichroic mirror reflects all incoming light up to 495 nm.

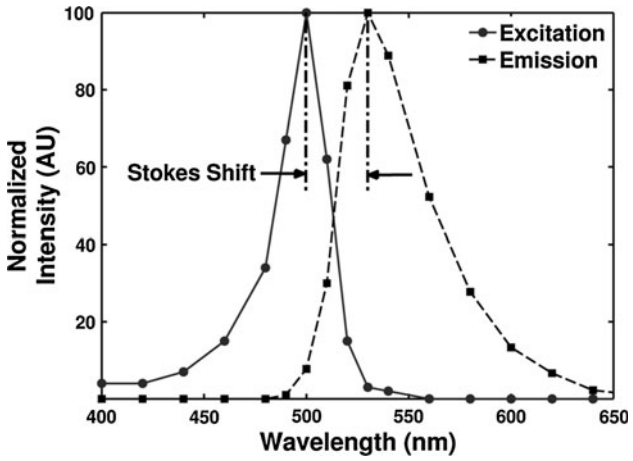

Fig. 9 Excitation and emission spectrum for Pyrromethene 556 (Exciton). The Stokes shift is the difference between maximum emission (540 nm) and maximum absorption (495 nm) wavelengths and is responsible for the visually discernible blue-to-green color change characteristic

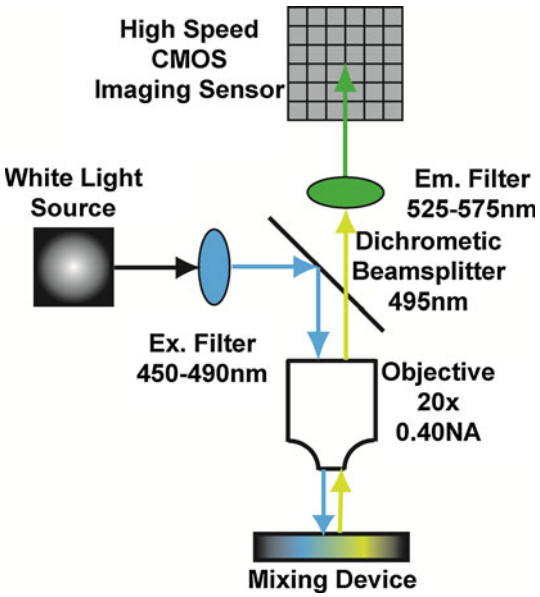

Fig. 10 Epi-fluorescent filter setup used for the Pyrromethene 556 LIF mixing measurements using a 200W white light source. Following a 470/20-nm band pass filter, the light is reflected by a 495-nm dichroic mirror, fills the back aperture of a ×20 objective, and illuminates the sample. Fluorescent emission passes back through the objective, the dichroic mirror, and a 550/25-nm band pass filter before being recorded on a high-speed CMOS array

The excitation light fills the back aperture of the microscope objective and illuminates the sample. The fluorescent emission, reflected excitation, and background light are subsequently routed back through the objective. The dichroic mirror transmits all light greater than 495 nm and the emission filter transmits light between 525 and 575 nm. The filtered signals are captured and recorded on a high-speed complementary metal–oxide–semiconductor (CMOS) camera (Photron SA5, 1,024 × 1,024 pixel array, 20 μm/pixel) that is coupled directly with a microscope optical port. A 200W metal-halide light (Prior Scientific Lumen 200) was used as the excitation source for these experiments. An extra-long working distance (ELWD) Plan Fluor 20× objective with a 0.40 numerical aperture was used for optical magnification.

The spatial resolution of this experimental setup is determined by the microscope objective, the physical size of the camera imaging sensor, and the exposure time used to capture the images. The microscope objective used for these experiments provides an in-plane and out-of-plane spatial resolution of 0.67 and 3.4 μm, respectively. The physical size of each pixel on the imaging sensor is 20 μm, which, at 20× magnification, provides an in-plane spatial resolution of 1 μm. The exposure time controls how long the imaging sensor is gathering fluorescent emission data for each image. As the exposure duration is increased, the image intensity increases proportionally but highly dynamic events become blurred and difficult to resolve. The in-plane spatial resolution is therefore the product of the anticipated system velocity and exposure duration. For example, capturing a particle traveling at 1 m/s with an exposure of 1 μs provides an in-plane spatial resolution of 1 μm. The resulting in-plane spatial resolution of the measurement system is the maximum of these three sources. For the results presented in the following section, the in-plane spatial resolution ranged from 2 to 21 μm and was limited by the 25-μs exposure used for image capture. Long exposure times were necessary in order to capture sufficient fluorescent intensity and utilize the full dynamic range of camera. The spatial resolution can be significantly improved by replacing the mercury halide light source used to initiate the LIF process with a high energy, high-repetition-rate laser. The temporal resolution of this measurement system is determined by the frame rate of the camera. Although the time between image frames can be arbitrarily long, it cannot be shorter than the camera exposure. Higher frame rates, and hence temporal resolution, are therefore limited by the camera exposure interval. Since the timescales of interest here are in the millisecond range, using a 20 kHz image frame rate, or a 50-μs imaging interval, provides sufficient temporal resolution.

The images captured with this experimental setup represent a two-dimensional slice of the droplet volume with a thickness equal to the 3.4-μm out-of-plane resolution. Fluorescent emission and noise originating from outside the depth of field are essentially averaged over a large area of pixels. Consequently, any information about out-of-plane intensity gradients is consequently lost. If out-of-plane gradients are expected, the numerical aperture and magnification of the objective can be reduced to increase

the depth of field. The concentration fields for the results to follow were expected to be primarily two dimensional, and care was taken to position the image plane in the center of the channel.

5 Results

Mixing dynamics in colliding droplets are examined using this optical diagnostic technique. Two droplets of high (0.8 mg/mL, $c^* \sim 1.5$) and low (0.08 mg/mL, $c^* \sim 0.15$) Pyrromethene 556 concentration are collided at a Y-junction. The two liquid streams from where the droplets originate are prepared using 0.2-μm filtered, steam distilled water. Litmus measurements of each mixture prior to injection into the mixing device showed a common pH of 7. Uniform pH is important because fluorescent emission of Pyrromethene dyes is sensitive to solution pH, particularly in acidic surroundings (Yariv and Reisfeld 1999). A common pH between the colliding droplets ensures that changes in fluorescent emission are due only to changes in concentration. Channel geometry used for these experiments is captured by the CAD image in Fig. 7. The 12 bit (4,096 intensity levels) monochromatic images were captured using an exposure and frame rate of 25 μs and 20,000 fps, respectively, and converted to double precision intensity images for statistical analysis.

Of the many collisions cataloged, three representative cases are presented that highlight how mixing is influenced by droplet inertia. The *Re* numbers considered are 7, 31, and 74 with corresponding convective timescales of 2, 0.5, and 0.1 ms. The viscous timescales remained relatively constant at 13, 17, and 8 ms, respectively. These three cases are denoted as Collision 1 (low *Re* number, long convective timescale), Collision 2 (mid *Re* number, mid convective timescale), and Collision 3 (high *Re* number, short convective timescale). The length scales and velocity values used to formulate the collision *Re* number and convective and viscous timescales for each collision are established using the images just prior to droplet collision. The length scale for each droplet is determined based on the number of non-zero pixel values appearing in the binary ROI mask. A collision length scale is then calculated using the following expression:

$$L_{\text{Collision}} = 2\frac{L_{\text{Droplet1}}L_{\text{Droplet2}}}{L_{\text{Droplet1}} + L_{\text{Droplet2}}} \tag{15}$$

For two equally sized droplets, the collision length scale is equal to the individual droplet length scale. As any one of the length scales approaches infinity, the collision length scale approaches twice the value of the finite scale. Since the interest here is mixing due to droplet collisions, the collision length scale is the characteristic length of the mixing process. The length scales for these three cases varied by less than a factor of two. The collision velocity is determined by the relative velocity between the two droplets at the time of collision. Droplet velocity is determined by pixel displacement, pixel size, and image frame rate. The collision velocity ranged from 0.06 to 0.8 m/s. Changes in the collision *Re* number and convective timescale are consequently due to changes in droplet inertia as opposed to length scale differences. A summary of these collision parameters is provided in Table 1.

The mixing statistics given by Eqs. 12 and 14 are calculated for each image frame and are based only on the non-zero pixel locations appearing in the binary ROI mask. The mixing time listed in Table 1 is determined by the temporal trend of the normalized standard deviation of the droplet intensity field. In order to track the progress of mixing and clearly identify a mixing timescale, a mixing parameter η is derived that is based on the normalized standard deviation for each image frame and scaled by the initial and steady-state values:

$$\eta = \frac{\frac{\sigma}{\mu_t} - \frac{\sigma}{\mu_\infty}}{\frac{\sigma}{\mu_0} - \frac{\sigma}{\mu_\infty}} \tag{16}$$

The initial and steady-state values used to formulate η correspond to the last frame just prior to droplet impact and the last frame where σ/μ becomes invariant with time. Cast in these terms, this mixing parameter begins at unity and asymptotically approaches zero as mixing progresses. Dynamic mixing within the sub-second timescales considered is assumed complete when η reaches 0.1 or is within 90 % of its steady-state value.

The time trace for σ/μ and η is shown in Figs. 11 and 12, respectively. Each case shows different mixing rates and steady-state values. The standard deviation of the intensity field provides a measure of mixedness for each captured

Table 1 Measured (length, velocity, mixing time) and calculated (Reynolds number, convective time scale) collision parameters for the three mixing events

Mixing event	Collision length (μm)	Collision velocity (m/s)	Reynolds number	Convective time (ms)	Mixing time (ms)
Collision 1	115 ± 1	0.06 ± 0.001	7 ± 0.7	1.99 ± 0.04	5.05 ± 0.85
Collision 2	129 ± 3	0.24 ± 0.006	31 ± 3	0.53 ± 0.02	4.10 ± 0.25
Collision 3	89 ± 11	0.83 ± 0.10	74 ± 6	0.11 ± 0.02	1.50 ± 0.55

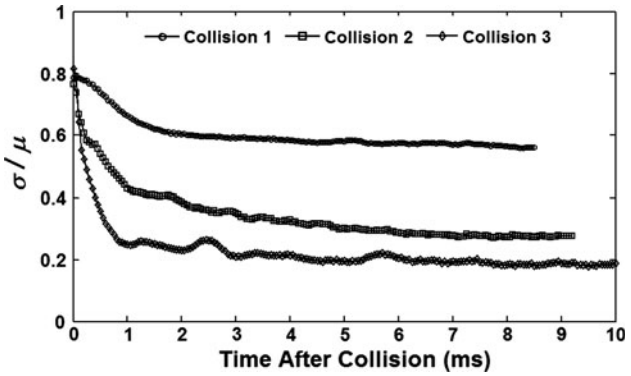

Fig. 11 Temporal changes in normalized standard deviation of the intensity field given by Eq. 12 for the three collision cases described in Table 1. Time begins at the last frame just prior to droplet collision. The data show collisions with short convective timescales produce lower standard deviations of the concentration field. A smaller ending standard deviation implies better mixed conditions

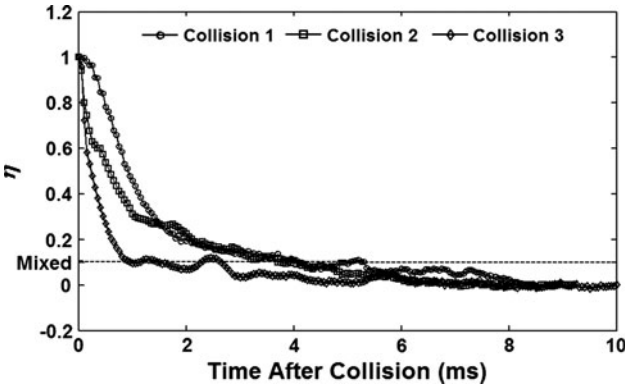

Fig. 12 Temporal changes in the mixing parameter η given by Eq. 16 for the three collision cases outlined in Table 1. Time begins at the last frame just prior to droplet collision and mixing is assumed complete when the mixing parameter reaches 0.1, as indicated by the dashed line. The data show that homogenization of the concentration field occurs faster for collisions with shorter convective timescales

image frame. The statistic decreases from its initial value just prior to collision and achieves a new value that remains relatively invariant under the timescales considered. The results show decreased intensity residuals for collisions occurring at higher relative velocities where increased rearrangement occurs. This is supported by inspection of the simple images shown in Fig. 4 and resulting standard deviation traces in Fig. 5. Note that, for a given number of diffusive averages, the standard deviation is significantly less if starting from a more rearranged state.

The decay rate is an indication of how quickly diffusion is homogenizing the concentration field. The rate is faster if diffusion begins from a more rearranged state since the number of interfaces is greatly increased. Collisions occurring at higher relative velocity produce greater volumetric rearrangement, that is, analogous to shaking a can of marbles with greater vigor. The kinetic energy carried by each droplet is viscously dissipated through complex velocity gradients within the liquid volume that help create concentration interfaces for mass diffusion. The length scale of the collision also plays an important role. When shaken at the same rate, a single marble is more likely to sample the entire can volume as compared to the same marble in a much larger can. This difference is captured by the convective timescale of the event. The ratio of actual mixing time to the convective timescale of the collision provides a convenient measure to distinguish the role of convective stirring in mixing. This ratio increased non-linearly with *Re* number from 2.5 for Collision 1 to 13.8 for Collision 3 as shown in Fig. 13 and supports the trend of results previously obtained for a different collision geometry (Carroll and Hidrovo 2012).

The other mixing statistic of interest is the average local intensity gradient given by Eq. 14. Recall that this statistic is an assessment of the diffusive interfaces available and larger values signify smaller local diffusion length scales and a greater potential for diffusive mixing. In order to compare the three collision cases, the average local gradient given by Eq. 14 is modified to a reduced form:

$$\phi = \frac{\Phi_t - \Phi_\infty}{\Phi_0 - \Phi_\infty} \tag{17}$$

Reducing the average gradient in this manner shows the number of interfaces that are created relative to the initial and final value. This is valuable information since one of the objectives of this diagnostic technique is to compare collisions at different inertial conditions and collision geometries. Collisions that produce large increases in concentration gradients should also display fast homogenization rates due to the reduced local diffusive length

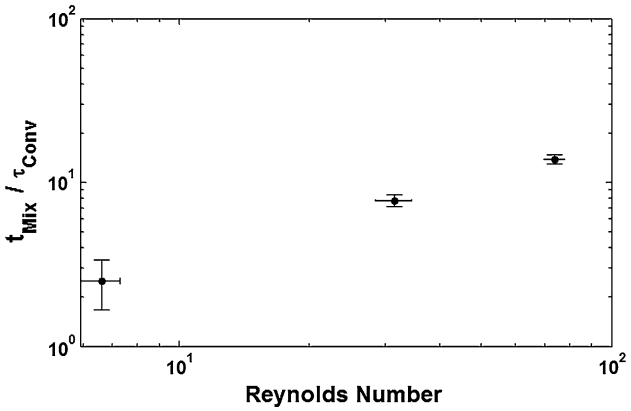

Fig. 13 Ratio of actual mixing time to the convective timescale for the three collision cases described in Table 1 versus the Reynolds number for the collision. *Error bars* are based on the spatial and temporal resolution of each collision case

scales. Although the time and length scale at which each operate are different, convective stirring and diffusion act in concert. Convection acts at the system level to create interfaces while diffusion acts at local level to smear these available interfaces. It is therefore expected that collisions involving short convective timescales will display larger initial changes in the average gradient statistic. Increases may be short lived, however, since a large number of available interfaces will activate diffusion and quickly reduce the statistic. The time trace for the reduced average gradient given by Eq. 17 is shown in Fig. 14 for the three collision cases outlined in Table 1. Collisions occurring at higher velocity elicit significantly more dynamic behavior, characterized by repeated increases and decreases in local gradients. This is clear by comparing the benign increase and gradual decrease for Collision 1 to the abrupt increase and subsequent decrease for Collision 2. The initial increase is greatest for Collision 3, which occurred at the highest *Re* number and shortest convective timescale. The change in the average gradient was smallest for Collision 1 and implies that the creation of interfaces due to volumetric rearrangement was not as significant compared with collisions occurring at larger *Re* numbers. The response shown by Collision 3 may also suggest three-dimensional flow field interactions, where fluid originating from outside the depth of field direction is brought into and out of view. Collisions occurring at large *Re* numbers should reveal complex 3D motion as the kinetic energy is dissipated. If material is convected into and out of the field of view, the average concentration within the depth of field is not necessarily conserved quantity. Reviewing the average concentration trace for Collision 3 shows a maximum concentration residual of 5 %, which occurs during the first millisecond of the collision event. Additional experiments

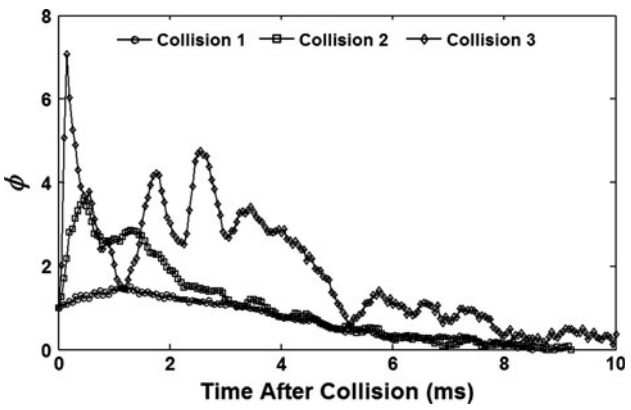

Fig. 14 Temporal changes in the reduced average intensity gradient parameter ϕ given by Eq. 17. Collisions occurring at higher relative velocity, such as Collision 3, are subject to greater volumetric rearrangement as indicated by the more dynamic time trace—larger gradients are being generated by convection and smeared by diffusion

are required to understand this behavior, such as relocating the image plane or using a lower numerical aperture objective and examining the resulting time traces for comparable hydrodynamic conditions.

Visualization remains invaluable for understanding mixing dynamics and resulting statistics. Applying a pseudo color map to the concentration field provides visual confirmation of mixing progress and identifies dynamics not readily evident using grayscale images alone. The pseudo coloring technique applied here is based not on actual intensity but on the deviation between actual and mean intensity, thereby providing a visual assessment of the mixing residuals. A custom color map is then applied that ranges from blue (locally unmixed) to red (locally mixed) and passes through the colors cyan, yellow, and orange. Furthermore, these images help highlight small differences in intensity more effectively than gray scale images. The images shown in Figs. 15, 16, and 17 correspond to Collision 1, 2, and 3 respectively.

Comparison of the three collisions cases show greater homogenization as the Reynolds number is increased. Collision 3 is significantly redder than the other cases and supports the steady-state values for the standard deviations given in Fig. 11. The images for the Collision 1 case show noticeable persistence of a concentration island located in the upper right portion of the droplet, and there is little change in the concentration residuals after 5 ms. Collision 2 shows two distinct islands that are separated by a nearly vertical interface that becomes pinned to the Y-junction apex at 1.5 ms. Convective motion for Collision 2 is confined to the right-most island while less mixing little takes place in the lower left portion of the droplet. Unlike to other two cases, Collision 3 shows extensive mixing throughout the droplet volume with no noticeable islands. The most interesting qualitative result that is shared by each collision case is the formation of a concentration "jet" that is released following the collision and is turned by the droplet boundaries. This is evident at 1 ms for Collision 1 and 0.5 ms for Collision 2. For the faster mixing collision, vortical motion is clearly visible and sustained throughout the mixing event and is responsible for the large average gradient statistic shown in Fig. 14. Vortices effectively stir the droplet contents and provide an increased number of concentration interfaces for diffusion to act leading to better droplet homogenization once collision dynamics subside.

6 Conclusion

Quantifying mixing rates in microchannel droplet flows remains a formidable task. The difficulty is compounded further when highly dynamic events such as droplet collisions

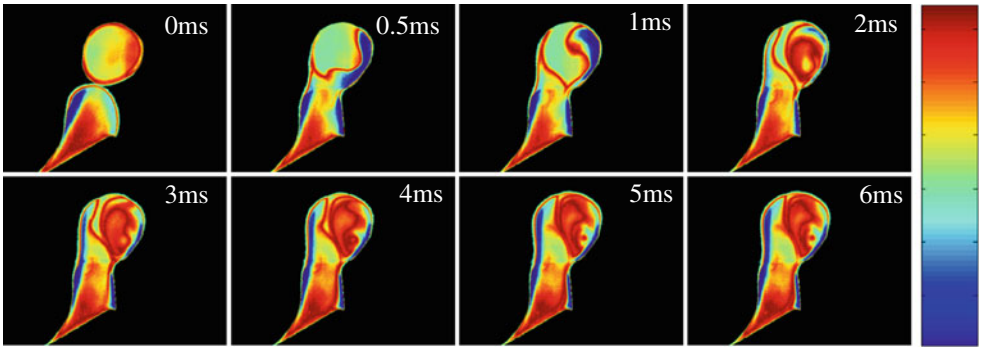

Fig. 15 Colored images of the Collision 1 mixing event ($Re = 7$, $\tau_{Conv} = 2$ ms) that have been pseudo-colored based on mixing residuals (difference between actual intensity and intensity when fully mixed) where red indicates locally mixed while blue indicates locally unmixed. Note the presence of islands that are not actively participating in the mixing process. The majority of active mixing takes place along the upper boundaries of the coalesced droplet

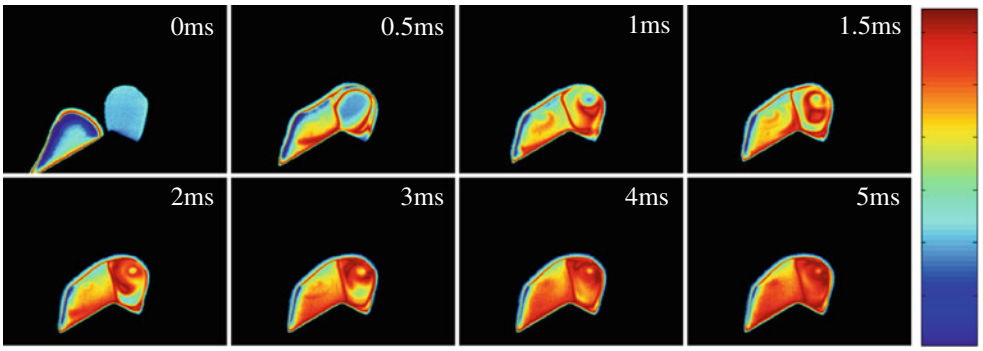

Fig. 16 Colored images of the Collision 2 mixing event ($Re = 31$, $\tau_{Conv} = 0.5$ ms) that have been pseudo-colored based on mixing residuals (difference between actual intensity and intensity when fully mixed) where *red* indicates locally mixed while blue indicates locally unmixed. A single vortex develops in the upper right portion of the droplet around 1 ms. Although the volume in the immediate vicinity of the vortex is well stirred around 4 ms, the left-most region remains largely unmixed

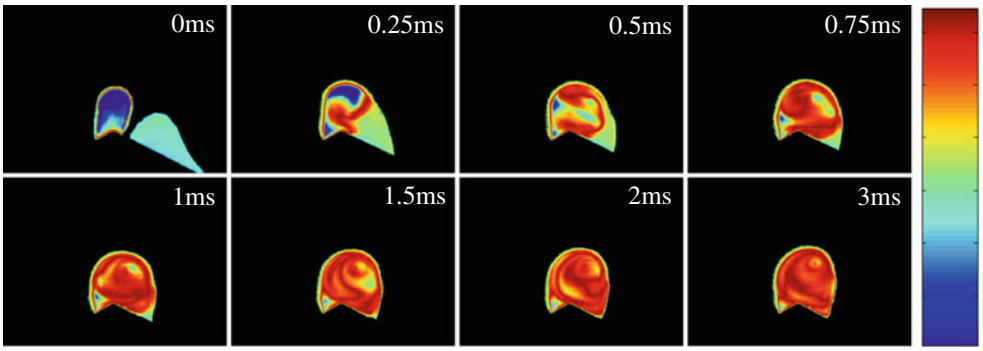

Fig. 17 Colored images of the Collision 3 mixing event ($Re = 74$, $\tau_{Conv} = 0.1$ ms) that have been pseudo-colored based on mixing residuals (difference between actual intensity and intensity when fully mixed) where *red* indicates locally mixed while blue indicates locally unmixed. Note the development of a single vortex at the center of the droplet around 1 ms that effectively stirs the droplet contents

are investigated. This manuscript described the development of a diagnostic framework that enables direct comparison of different hydrodynamic conditions and microchannel geometries on droplet mixing performance. The diagnostic technique was stimulated by a need to characterize and improve mixing rates for a new generation of droplet-based mixing devices. These devices utilize high-speed droplet collisions in confined microchannel geometries to quickly mix nanoliter-sized droplets. The measurement technique employs epi-fluorescent microscopy, high-speed image acquisition, and unique image processing operations that provide a statistical interpretation of the mixing process. The mixing of interest is the homogenization of a scalar field generated by laser-induced fluorescence. No chemical

reactions are employed, and no attempt is made to resolve molecular scale proximity of the diffusing species.

Two statistics are calculated for each captured image frame, and the temporal behavior of these statistics is used to measure the duration of the mixing event and help separate the inherently simultaneous action of bulk convective stirring and mass diffusion. The global standard deviation monitors the role of tracer diffusion while the local average intensity gradient is used to examine the influence of the convective rearrangement process. The diagnostic technique was exercised for three representative collision cases. The droplet collision Reynolds numbers considered ranged from 7 to 74 with convective timescales from 2 to 0.1 ms. The collision length scale varied only by a factor of two such that the majority of change in the collision Reynolds number was due to changes in collision velocity, which ranged from 0.06 to 0.8 m/s. The duration of the dynamic mixing event ranged from 5 to 1.5 ms. As anticipated, collisions occurring at higher relative velocities but similar length scales displayed faster mixing times and better homogenization. The collision velocity also produced significant differences in the initial response of the average concentration gradient. The higher speed collisions displayed an initially rapid increase in the average concentration gradient that indicated effective stirring and rearrangement of the droplet contents. Visual investigation of the mixing event identified the presence of vortices inside the newly coalesced droplets for each collision case examined. The duration of these vortices was greatest for the highest velocity collision and resulted in faster mixing time and improved spatial homogenization.

The spatial resolution of this diagnostic technique ranged from 2 to 21 μm and was undoubtedly limited by the light source used to excite the fluorophores and the sensitivity of the high-speed camera used to capture the emission. As the collision velocity is increased, the in-plane spatial resolution decreases proportionally unless the camera exposure time is reduced. Reducing the camera exposure time, however, decreases the captured fluorescent emission signal. The spatial resolution can potentially be increased to the size of the camera pixel by using a high-repetition, high-power laser. The out-of-plane resolution was limited to 3.4 μm for these experiments but can be increased or decreased by changing the numerical aperture of the microscope objective. Three-dimensional effects can no longer be discounted as the collision velocity is increased, and the nominally two-dimensional slice provided this objective may prove insufficient at larger Reynolds numbers. The three cases examined here illicit predominately two-dimensional flow field but the possibility out-of-plane effects are beginning to materialize for the highest velocity collision.

Acknowledgments This work was supported by DARPA 2008 Young Faculty Award (YFA) grant HR0011-08-1-0045 and is currently being supported by an NSF CAREER Award grant CBET-1151091.

References

Anderson P, Bath A, Groger W, Lulf HW, Meijer G, Meulen JJt (1998) Laser-induced fluorescence with tunable excimer lasers as a possible method for instantaneous temperature field measurements at high pressures: checks with atmospheric flame. Appl Opt 27:365–378

Arbeloa FL, Arbeloa TL, Arbeloa IL, Moreno IG, Costela A, Sastre R, Amat-Guerri F (1998) Photophysical and lasing properties of pyrromethene 567 dye in liquid solution. Chem Phys 236:331–341

Arbeloa FL, Banuelos J, Martinez V, Arbeloa T, Arbeloa IL (2005) Structural, photophysical and lasing properties of pyrromethene dyes. Int Rev Phys Chem 24:339–374

Aref H (1984) Stirring by chaotic advection. J Fluid Mech 143:1–21. doi:10.1017/S0022112084001233

Bellerose JA, Rogers CB (1994) Measuring mixing and local pH through laser induced fluorescence. Laser Anemometry 191:217–220

Borlinghaus R (2011) The white confocal: continuous spectral tuning in excitation and emission. In: Diaspro A (ed) Optical fluorescence microscopy. Springer, New York, pp 37–54

Carroll B, Hidrovo C (2009) An experimental investigation of droplet detachment in high-speed microchannel air flow. In: 2nd ASME micro/nanoscale heat & mass transfer international conference, Shanghai, China, December 18–21, 2009

Carroll B, Hidrovo C (2010) Quantification of inertial droplet collision mixing rates in confined microchannel flows using differential fluorescence measurements. In: 8th ASME international conference on nanochannels, microchannels, and minichannels, Montreal, Canada, August 1–5, 2010

Carroll B, Hidrovo C (2011) Experimental investigation of inertial mixing in droplets. In: 9th ASME international conference on nanochannels, microchannels, and minichannels, Edmonton, Alberta, Canada, June 19–22, 2011

Carroll B, Hidrovo C (2012) Experimental investigation of inertial mixing in colliding droplets. Heat Transf Eng. doi:10.1080/01457632.2013.703087

Coppeta J, Rogers C (1998) Dual emission laser induced fluorescence for direct planar scalar behavior measurements. Exp Fluids 25:1–15. doi:10.1007/s003480050202

Coppeta J, Rogers C, Philipossian A, Kaufman FB (1996) Characterizing slurry flow during CMP using laser induced fluorescence. In: Workshop on chemical mechanical polishing, Lake Placid

David M, Fogg D, Hidrovo C, Flynn R, Goodson K (2006) Development and calibration of a two-dye fluorescence system for use in two-phase micro flow thermometry

Dimotakis PE (2005) Turbulent mixing. Annu Rev Fluid Mech 37:329–356. doi:10.1146/annurev.fluid.36.050802.122015

Dimotakis PE, Miake-Lye RC, Papantoniou DA (1983) Structure and dynamics of round turbulent jets. Phys Fluids 26:3185–3192

Dutta P, Chevray R (1994) Inertial effects in chaotic mixing with diffusion. J Fluid Mech 285:1–16

Faes M, Glasmacher B (2010) Anlaysis of macro and micromixing in laminar stirred mixing vessels using laser optical and numerical methods. In: Bockhorn H, Peukert W, Mewes D, Warnecke HJ (eds) Macro and micro mixing: analysis, simulation and numerical calculation. Springer, Berlin, pp 55–67

Hertzog DE, Michalet X, Jager M, Kong X, Santiago JG, Weiss S, Bakajin O (2004) Femtomole mixer for microsecond kinetic studies of protein folding. Anal Chem 76:7169–7178. doi:10.1021/ac048661s

Hertzog DE, Ivorra B, Mohammadi B, Bakajin O, Santiago JG (2006) Optimization of a microfluidic mixer for studying protein folding kinetics. Anal Chem 78:4299–4306. doi:10.1021/ac051903j

Hidrovo CH, Hart DP (2001) Emission reabsorption laser induced fluorescence (ERLIF) film thickness measurement. Meas Sci Technol 12:467–477

Hiller B, Hanson RK (1988) Simultaneous planar measurements of velocity and pressure fields in fas flows using laser-induced fluorescence. Appl Opt 27:33–48

Jacobs B, Gekelman W, Pribyl P, Barnes M, Kilgore M (2007) Laser-induced fluorescence measurements in an inductively coupled plasma reactor. Appl Phys Lett 91:161503–161505

Jendrzok B, Pauls C, Kob HJ, Lucas K (2010) Time-resolved measurement of concentrations in mixing processes using Raman spectroscopy. In: Bockhorn H, Peukert W, Mewes D, Warnecke HJ (eds) Micro and macro mixing: analysis, simulation and numerical calculation. Springer, Berlin, pp 39–53

Kinsey JL (1977) Laser-induced fluorescence. Ann Rev Phys Chem 28:349–372

Kling K, Mewes D (2010) Measurements of macro and micro-scale mixing by two-color laser induced fluorescence. In: Bockhorn H, Peukert W, Mewes D, Warnecke HJ (eds) Macro and micro mixing: analysis, simulation and numerical calculation. Springer, Berlin, pp 55–67

Knight JB, Vishwanath A, Brody JP, Austin RH (1998) Hydrodynamic focusing on a silicon chip: mixing nanoliters in microseconds. Phys Rev Lett 80:3863–3866

Koochesfahani MM, Dimotakis PE (1986) Mixing and chemical reactions in a turbulent liquid mixing layer. J Fluid Mech 170:83–112. doi:10.1017/S0022112086000812

Lavieille P, Lemoine F, Lavergne G, Lebouché M (2001) Evaporating and combusting droplet temperature measurements using two-color laser-induced fluorescence. Exp Fluids 31:45–55. doi:10.1007/s003480000257

MacDonald RI (1990) Characteristics of self-quenching of the fluorescence of lipid-conjugated rhodamine in membranes. J Biol Chem 265:13533–13539

Masca SI, Rodriguez-Mendieta IR, Friel CT, Radford SE, Smith DA (2006) Detailed evaluation of the performance of microfluidic T mixers using fluorescence and ultraviolet resonance Raman spectroscopy. Rev Scient Instrum 77:055105–055109

Matsumoto K, Fujii T, Suzuki K, Segawa D, Kadota T (1999) Laser induced fluorescence for the non-intrusive diagnostics of a fuel droplet burning under microgravity in a drop shaft. Meas Sci Technol 10:853–858

Nguyen N-T (2008) Micromixers fundamentals, design and fabrication. William Andrew Inc., Norwich

Ottino J (1989) The kinematics of mixing: stretching, chaos, and transport. Cambridge University Press, Cambridge

Ottino JM (1990) Mixing, chaotic advection, and turbulence. Annu Rev Fluid Mech 22:207–253

Ottino JM (1994) Mixing and chemical reactions a tutorial. Chem Eng Sci 49:4005–4027

Ottino JM, Wiggins S (2004) Introduction: mixing in Microfluidics. Philos Trans R Soc Lond A 362:923–935

Park HY, Kim SA, Korlach J, Rhoades E, Kwok LW, Zipfel WR, Waxham MN, Webb WW, Pollack L (2007) Conformational changes of calmodulin upon Ca^{2+} binding studied with a microfluidic mixer. Proc Nat Acad Sci USA 105:542–547

Quercioli F (2011) Fundamentals of optical microscopy. In: Diaspro A (ed) Optical fluorescence microscopy. Springer, New York, pp 1–36

Robinson T, Manning HB, Dunsby C, Neil MAA, Baldwin GS, deMello AJ, French PM (2010) Investigating fast enzyme-DNA kinetics using multidimensional fluorescence imaging and microfluidics. In: Proceedings of SPIE, San Francisco

Schrader B, Hoffmann A, Keller S (1991) Near-infrared fourier transform raman spectroscopy: facing absorption and background. Spectrochim Acta A 47:1135–1148

Shah M, Thangaraj K, Soong M-L, Wolford LT, Boyer JH, Politzer IR, Pavlopoulos TG (1990) Pyrromethene–BF2 complexes as laser dyes. Heteroat Chem 1:389–399. doi:10.1002/hc.520010507

Simpson SF, Kincaid JR, Holler FJ (1983) Microdroplet mixing for rapid reaction kinetics with Raman spectrometric detection. Anal Chem 55:1420–1422. doi:10.1021/ac00259a054

Simpson SF, Kincaid JR, Holler FJ (1986) Development of a microdroplet mixing technique for the study of rapid reactions by Raman spectroscopy. Anal Chem 58:3163–3166. doi:10.1021/ac00127a054

Song H, Ismagilov RF (2003) Millisecond kinetics on a microfluidic chip using nanoliters of reagents. J Am Chem Soc 125:14613–14619. doi:10.1021/ja0354566

Song H, Bringer MR, Tice JD, Gerdts CJ, Ismagilov RF (2003) Experimental test of scaling of mixing by chaotic advection in droplets moving through microfluidic channels. Appl Phys Lett 83:4664–4666. doi:10.1063/1.1630378

Song H, Chen DL, Ismagilov RF (2006) Reactions in droplets in microfluidic channels. Angew Chem Int Ed 45:7336–7356. doi:10.1002/anie.200601554

Takahashi S, Ching Y, Wang J, Rouseau DL (1995) Microsecond generation of oxygen-bound cytochrome c oxidase by rapid solution mixing. J Biol Chem 270:8405–8407

Ware WR (1962) Oxygen quenching of fluorescence in solution: an experimental study of the diffusion process. J Phys Chem 66:455–458. doi:10.1021/j100809a020

Yariv E, Reisfeld R (1999) Laser properties of pyrromethene dyes in sol-gel glasses. Opt Mater 13:49–54